frontiers | Frontiers in Earth Science

TYPE Original Research
PUBLISHED 20 April 2023
DOI 10.3389/feart.2023.1063922

OPEN ACCESS

EDITED BY
Ryunosuke Kazahaya,
National Institute of Advanced Industrial Science and Technology (AIST), Japan

REVIEWED BY
Jian Xu,
Chinese Academy of Sciences (CAS), China
Toshiya Mori,
The University of Tokyo, Japan

*CORRESPONDENCE
Alexander Nies,
alexander.nies@cnrs-orleans.fr

RECEIVED 07 October 2022
ACCEPTED 04 April 2023
PUBLISHED 20 April 2023

CITATION
Nies A, Heimann J, Fuchs C, Kuhn J, Bobrowski N and Platt U (2023), Quantifying BrO and SO_2 distributions in volcanic plumes—Recent advances in imaging Fabry-Pérot interferometer correlation spectroscopy.
Front. Earth Sci. 11:1063922.
doi: 10.3389/feart.2023.1063922

Quantifying BrO and SO_2 distributions in volcanic plumes—Recent advances in imaging Fabry-Pérot interferometer correlation spectroscopy

Alexander Nies[1,2]*, Jaro Heimann[1], Christopher Fuchs[1,3], Jonas Kuhn[1], Nicole Bobrowski[1,4] and Ulrich Platt[1]

[1]Institute of Environmental Physics, Heidelberg University, Heidelberg, Germany, [2]Laboratoire de Physique et de Chimie de l`Environnement et de l`Espace, CNRS/University Orleans, Orleans, France, [3]Institute for Atmospheric and Climate Science, ETH Zurich, Zurich, Switzerland, [4]Istituto Nazionale di Geofisica e Vulcanologia—Osservatorio Etneo, Catania, Italy

Bromine monoxide (BrO) and sulphur dioxide (SO_2) are two gases frequently observed in volcanic plumes by spectroscopic techniques capable of continuous gas monitoring like, e.g., Differential Optical Absorption Spectroscopy (DOAS). The spatio-temporal resolution of DOAS measurements, however, only allows to determine average gas fluxes (minutes to hours resolution). In particular, it is insufficient to record two-dimensional images of SO_2 and BrO in real-time (seconds time resolution). Thus, it is impossible to resolve details of chemical conversions of reactive plume constituents. However, these details are vital for further understanding reactive halogen chemistry in volcanic plumes. Therefore, instruments that combine high spatio-temporal resolution and high gas sensitivity and selectivity are required. In addition, these instruments must be robust and compact to be suitable for measurements in harsh and remote volcanic environments. Imaging Fabry-Pérot interferometer (FPI) correlation spectroscopy (IFPICS) is a novel technique for atmospheric trace gas imaging. It allows measuring atmospheric gas column density (CD) distributions with a high spatial and temporal resolution, while at the same time providing selectivity and sensitivity comparable to DOAS measurements. IFPICS uses the periodic transmission spectrum of an FPI, that is matched to the periodic narrowband (vibrational) absorption features of the target trace gas. Recently, IFPICS has been successfully applied to volcanic SO_2. Here we demonstrate the applicability of IFPICS to much weaker (about two orders of magnitude) trace gas optical densities, such as that of BrO in volcanic plumes. Due to its high reactivity, BrO is extremely difficult to handle in the laboratory. Thus, based on the similarity of the UV absorption cross sections, we used formaldehyde (HCHO) as a spectral proxy for BrO in instrument characterization measurements. Furthermore, we present recent advances in SO_2 IFPICS measurements and simultaneous measurements of SO_2 and BrO from a field campaign at Mt Etna in July 2021. We find photon shot-noise limited detection limits of 4.7×10^{17} molec $s^{0.5}$ cm^{-2} for SO_2 and of 8.9×10^{14} molec $s^{0.5}$ cm^{-2} for BrO at a spatial resolution of 512 × 512 pixels and 200 × 200 pixels, respectively. Furthermore, an estimate for the BrO to SO_2 ratio (around 10^{-4}) in the volcanic plume is given. The prototype instrument presented here provides spatially resolved measurements of the reactive volcanic plume component BrO. The

temporal resolution of our approach allows studies of chemical conversions inside volcanic plumes on their intrinsic timescale.

KEYWORDS

remote sensing, Fabry-Perot interferometer, imaging, bromine monoxide, sulphur dioxide, volcanic plumes, IFPICS

1 Introduction

Despite of their low atmospheric mixing ratios, halogen radicals substantially influence atmospheric processes and impact the overall oxidative capacity of the atmosphere. Several volcanoes are strong sources yielding comparatively high atmospheric mixing ratios of halogen radicals (particularly bromine species) inside volcanic plumes (e.g., Bobrowski, et al., 2003). Bromine radicals influence the oxidation capacity of the atmosphere. For instance, they catalyze ozone (O_3) destruction, interfere with the NO_x-reaction cycle, and may enhance the hydroxyl radical to hydroperoxyl (OH/HO_2) ratio. Hypophalus acids like hypobromous acid (HOBr, formed from BrO) can accelerate the formation of sulphate in aqueous particles and bromine atoms can oxidize mercury and therefore reduce its atmospheric lifetime (e.g., Platt & Bobrowski 2015). Moreover, in the atmosphere near active volcanoes, bromine almost exclusively originates from the volcanoes itself, which additionally might make it a good tracer for volcanic activity (e.g., Platt & Bobrowski 2015). Therefore, it is of great interest to study the abundance and behavior of these species.

Ground based remote sensing techniques are a common tool to measure gases in volcanic plumes. SO_2 and BrO can be measured and continuously monitored readily by DOAS (see, e.g., Platt & Stutz 2008). However, the spatio-temporal resolution of typical DOAS instruments is too low to resolve fast chemical evolution processes. Beside the atmospheric impact, those processes need to be better understood in order to link, for example, the BrO amount in volcanic plumes to volcanological parameters (e.g., the bromine emission). The formation of BrO in the atmosphere is explained by the autocatalytic oxidation of bromide, also known as 'bromine explosion' (Platt & Lehrer 1997), which was found to occur in marine and polar boundary layers (Barrie et al., 1988), over salt lakes (Stutz et al., 2002) and also has been observed in volcanic plumes (Bobrowski et al., 2003). The presence of BrO in volcanic plumes has a number of consequences for atmospheric chemistry, for instance O_3 destruction is catalyzed (e.g., Bobrowski et al., 2007; Vance et al., 2010).

Fast and spatially resolved measurements of BrO can yield important insights into the chemical processes occurring in volcanic plumes. An ideal instrument for such observations combines a high spatial resolution (on the order of meters) to resolve the spatial distribution of trace gas gradients and a high temporal resolution (on the order of seconds) for the observation of fast chemical conversions of trace gases. These properties should not come at the expense of high selectivity and sensitivity of the instrument towards the gas to be measured. Also, the instrument should be compact and robust to be operable in remote locations.

Here we present a prototype imaging instrument based on the IFPICS technology proposed by Kuhn et al. (2014) and applied to measure volcanic SO_2 distributions by Fuchs et al. (2021). It utilizes the periodic transmission spectrum of an FPI in a camera setup, which results in a high selectivity and sensitivity, while retaining high spatio-temporal resolution (see Section 2.1).

This work demonstrates the applicability of the IFPICS technology to atmospheric absorbers with—compared to SO_2—low differential optical densities (of the order of 10^{-3}) like BrO. We present imaging measurements of HCHO gas cells. Due to the similarity of the UV absorption cross sections, HCHO can serve as a spectral proxy for BrO absorption in characterization measurements. Furthermore, advances in SO_2 imaging and parallel imaging measurements of volcanic SO_2 and BrO performed at Mt Etna in July 2021 are presented and compared to DOAS measurements.

2 Materials and methods

2.1 Imaging Fabry-Pérot interferometer correlation spectroscopy (IFPICS)

IFPICS combines the benefits of line-scanning "hyperspectral" cameras (or imaging DOAS, see, e.g., Lohberger et al., 2004; Louban et al., 2009) and of filter-based cameras (like the "SO_2 camera," see, e.g., Mori & Burton 2006; Bluth et al., 2007) by using an FPI as a wavelength selective element. In other words, IFPICS combines high sensitivity and selectivity with high spatio-temporal resolution. The FPI and its transmission spectrum is designed to match periodic components of the absorption cross section of a target trace gas. This approach yields a much higher selectivity and sensitivity compared to filter-based cameras (see Kuhn et al., 2014; Kuhn et al., 2019; Fuchs et al., 2021 for details). Lambert-Beers law states that, the optical density of the target trace gas τ is given by the logarithmic ratio of the incoming radiance without the targeted trace gas absorption I_0 to the incoming radiance including trace gas absorption I, i.e., $\tau = \ln(I_0/I)$. Similar to trace gas detection with filter-based SO_2 cameras, IFPICS relies on recording spatial distributions of trace gas optical densities in two (or more) wavelength channels (obtained by tuning the FPI transmission spectrum). This concept is illustrated in Figure 1 for the trace gases BrO, HCHO, and SO_2. First, in an on-band channel "A" the transmission maxima of the FPI are tuned (by tilting the FPI element) to the absorption maxima of the target gas. The optical density τ_A is recorded when the FPI transmission exhibits maximum correlation with the narrowband absorption structure of the target trace gas (e.g., the vibrionic bands in the UV for SO_2 and BrO). Then, τ_A is compared to the optical density τ_B, recorded in an off-band channel "B," when the FPI transmission maxima are slightly tuned (shifted around 1–2 nm by tilting the FPI element) to coincide with the absorption minima of the target gas. In this setting, the FPI transmission anti-correlates with the absorption structure of the

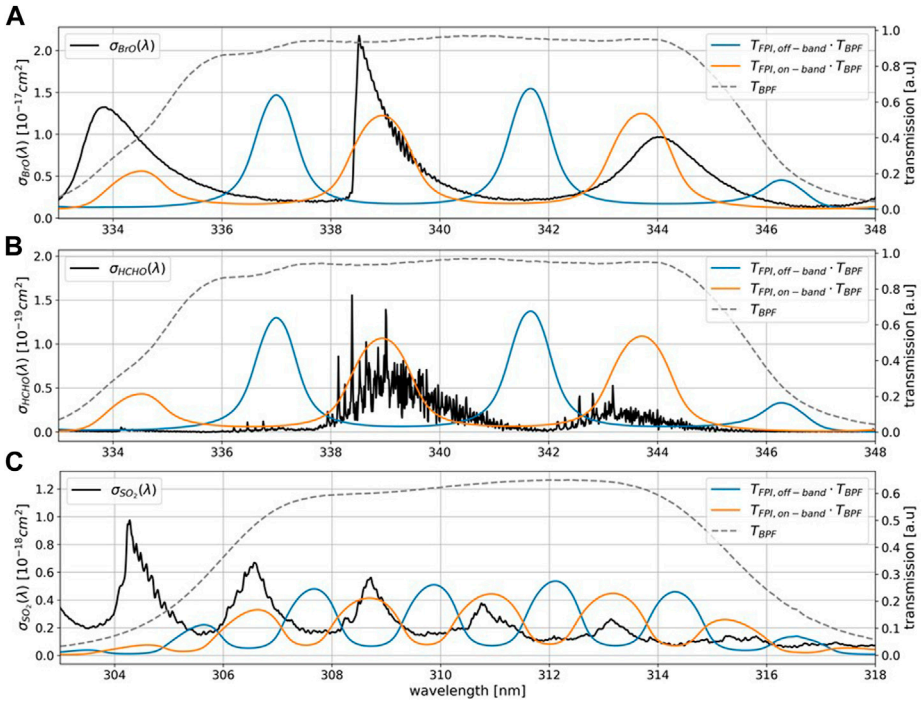

FIGURE 1
Trace gas detection principle of the IFPICS technique for BrO **(A)**, HCHO **(B)** and SO_2 **(C)**. The absorption cross sections σ_{BrO}, σ_{HCHO}, and σ_{SO2} of the trace gases are marked in black. The dashed line corresponds to the transmission curve of the broadband bandpass filter T_{BPF} with a central wavelength of 340 nm for BrO and HCHO and 310 nm for SO_2. The colored lines correspond to the FPI transmission spectrum T_{FPI} multiplied with the bandpass filter transmission in on-band position A (orange) and off-band position B (blue).

TABLE 1 Instrumental and optical parameters of both camera systems with uncertainties.

Parameter	SO_2 camera	BrO camera	Description
d [μm]	21.684 ± 0.002	12.366 ± 0.002	FPI mirror separation
R	0.65	0.70	FPI reflectivity
F	7.15	8.54	FPI finesse
n	1.00029	1.00029	Refractive index (air)
α_A [°]	8.35 ± 0.02	9.45 ± 0.02	FPI tilt, on-band
α_B [°]	6.80 ± 0.02	6.07 ± 0.02	FPI tilt, off-band
$T_{BPF,max}$	0.63	0.85	BPF peak transmission
λ_{BPF} [nm]	310.5	340.4	BPF central wavelength
δ_{BPF} [nm]	9.0	10.0	BPF FWHM
f [mm]	47 ± 2	47 ± 2	Lens system 1 focal length
a [mm]	1.60 ± 0.05	1.10 ± 0.05	Aperture diameter
Θ_{FOV} [°]	17	17	Imaging FOV

target trace gas. Differential evaluation (equivalent to rationing) of both channels yields the so-called apparent absorbance (AA). The AA is a quantity proportional to the target trace gas CD S. The instrument sensitivity k is determined by the difference of the mean weighted absorption cross sections $\bar{\sigma}_A$ and $\bar{\sigma}_B$ of the two wavelength channels, respectively:

$$AA = \tau_A - \tau_B = \ln\left(\frac{I_{A,0} I_B}{I_A I_{B,0}}\right) = (\bar{\sigma}_A - \bar{\sigma}_B) \cdot S = k \cdot S \quad (1)$$

Here I_A and I_B describe the incoming radiances with the target trace gas in the light path and $I_{A,0}$, $I_{B,0}$ the background radiances without the target trace gas absorption (i.e., pixels within the FOV that do not cover the volcanic plume). Matching of the transmission curve of the FPI to the periodicity of the target molecule is accomplished by choosing appropriate physical FPI parameters, i.e., choosing the mirror separation and the finesse (given essentially by the mirror reflectivity) of the FPI. An assessment of the signal to noise ratio gives an optimal finesse for the FPI (Kuhn et al., 2014). The two FPI positions (A, B, see above) are achieved by altering the angle of incidence on the FPI (α_A, α_B), in our case by about 3° for BrO and 1° for SO_2 (see Table 1). Additionally, a bandpass filter (BPF) is used to select the wavelength range (typically around 10 nm width) with high correlation between FPI transmission and absorption spectrum and low cross interferences. The choice of the FPI instrument parameters and wavelength windows is based on simulations by Kuhn et al., 2019.

The optical density of the individual spectral channels is not only sensitive to the absorption of the target trace gas, but also to extinctions resulting from scattering by aerosols and clouds, or by absorption of other trace gases. However, due to the small spectral shift (1–2 nm) of the FPI transmission between channels

A and B, broadband influences essentially cancel out in the evaluation. Furthermore, the selectivity achieved by the matched transmission spectrum of the FPI minimizes interferences with other trace gases absorbing in the same wavelength region.

2.2 The IFPICS instruments

The two IFPICS instruments (for BrO and SO_2, respectively, based on the design by Fuchs et al., 2021) used in this study are prototypes optimized for harsh environmental conditions and easy handling with compact dimensions of 200 mm × 350 mm × 130 mm, low weight of approximately 5 kg and a low power consumption (<10 W). The BrO and the SO_2 cameras are of the same design except for different FPIs and band-pass filters (see Section 2.1). The wavelength range for the SO_2 camera is (310 ± 5) nm and for the BrO camera (340 ± 5) nm. All instrumental parameters are summarized in Table 1.

Several improvements compared to the design of Fuchs et al., 2021 are introduced. 1) A major difference is the addition of a second optics next to the IFPICS optics to include a coaligned DOAS instrument with a narrow field of view (FOV) of 0.5° which is inside the FOV of the IFPICS instrument. It allows for a real-time SO_2 DOAS evaluation (see Luebcke et al., 2013) to trace the volcanic plume and to validate the model calibration (see Section 2.3). 2) We use a temperature-stabilized CMOS sensor (pco.edge bi 4.2 UV provided by Excelitas PCO GmbH) with a spatial resolution of 2048 × 2048 pixels. It allows for a time optimized acquisition of images, which results in a time resolution of ca. 2 Hz (BrO camera) and ca. 0.5 Hz (SO_2 camera). 3) The SO_2 camera BPF in Fuchs et al., 2021 was inclined by about 10° towards the optical axis. In the new SO_2 camera setup the filter was used without inclination. The operating wavelength range is thereby shifted by 2 nm towards higher wavelength, resulting in a more linear instrument response and higher photon yield. 4) The instrument software has been revised and optimized for field measurements.

The imaging optics are implemented as image side telecentric optics, with approximately uniform incidence angles of the incoming radiation on the FPI. This ensures that each pixel of the detector sees the same transmission spectrum on the FPI for the entire FOV. A detailed description of the instrument optics can be found in Fuchs et al., 2021. In principle, other optical setups are possible as discussed in Kuhn et al., 2014. Both cameras have a FOV of 17°. The spatial resolution for a given trace gas detection limit is limited by the FPI aperture size (Kuhn et al., 2019). The circular shape of the image aperture causes a circular image on the square detector area. In addition, the magnification of this image on the detector can be adjusted by the imaging optics and allows to shrink the imaging FOV to a reduced sensor area for low light conditions.

2.3 The instrument model

In order to convert the AA (see Eq. 1) into the trace gas CD S, we use the IFPICS instrument model as described in Fuchs et al., 2021. The model calculates the spectral instrument transmission, based on the FPI parameters and BPFs used in the camera setups. The radiances $I_0(\lambda)$ are taken from a solar atlas spectrum (Chance & Kurucz 2010) and are scaled with λ^{-4} to approximate a Rayleigh scattering atmosphere. Moreover, stratospheric O_3 absorption is included, as it governs the UV radiance that reaches Earth's surface at lower UV wavelengths, which particularly effects the SO_2 measurement. The absorption cross sections of O_3, SO_2, HCHO, and BrO are obtained from Serdyuchenko et al., 2014, Bogumil et al., 2003, Chance & Orphal 2011 and Fleischmann et al., 2004, respectively.

In order to determine the FPI tilt angles α_A and α_B (see Table 1), we calculate the integrated radiances $I_{FPI}(\alpha)$ containing the target trace gas absorption and the radiances $I_{0,FPI}(\alpha)$ without target trace gas absorption as a function of the incidence angle α (i.e., an interferogram). The progression of τ_{FPI} under variation of the incidence angle α of incoming radiation represents the shift of the FPI transmission across the trace gas absorption spectrum and allows to find the optimum FPI tilt angles (α_A and α_B) for on-band and off-band measurements, respectively. The modelled interferograms for BrO and HCHO are displayed in Figure 2. The optimal tilt angles for a measurement of BrO and HCHO are equal within the scale of the resolution of the stepper motor (0.02°). For optimal tilt angles, a calibration curve is calculated. The incidence angles are kept constant at α_A and α_B and the CD S of the target trace gas is varied, which gives the calibration curve from $AA_{FPI} = k \cdot S$. The instrument sensitivity k is determined by a linear fit for BrO and a polynomial fit for SO_2 of the calibration curve.

3 Results

3.1 Laboratory measurements of HCHO

As described above, we use the similarities of the BrO and HCHO spectral absorption in the instruments' operating wavelength range (335 nm–345 nm, see Figures 1A, B, 2) for the characterization of the BrO camera. HCHO is chemically more stable than BrO and thus easier to handle in the laboratory, e.g., in calibration cells. Thus, HCHO is used as a spectral proxy for BrO in order to characterize the instrument. The HCHO cell was prepared by initially filling a quartz cell with para-formaldehyde (PFA, produced by Sigma-Aldrich with an assay of 95.0%–100.5%), in the form of a white powder. It is then evaporated by heating the cell with a heat gun to form gaseous HCHO. During cooling the gaseous HCHO repolymerizes to PFA and settles on the walls of the gas cell. This leads to a gradually decreasing HCHO signal during the course of the experiment (e.g., shown with the various colors in Figure 3).

The instrument model (see Section 2.3; Figure 2) confirms that both gases can be detected with equal FPI instrument parameters. The modeled optimal angles α_A and α_B for the on- and off-band FPI setting (A, B) can be validated by recording an interferogram (the transmitted intensity for a continuous sequence of FPI tilt angles) of a HCHO gas cell. Such an interferogram of a HCHO gas cell where scattered skylight is used as a light source is presented in Figure 3. Here the mean value of the optical density τ within the gas cell is plotted as a function of the angle of incidence α of the collimated light beam on the FPI. The interferogram is recorded with a resolution of 0.2° in a range between 4° and 11.2°. This range is chosen as a trade-off between the effective finesse decrease for higher

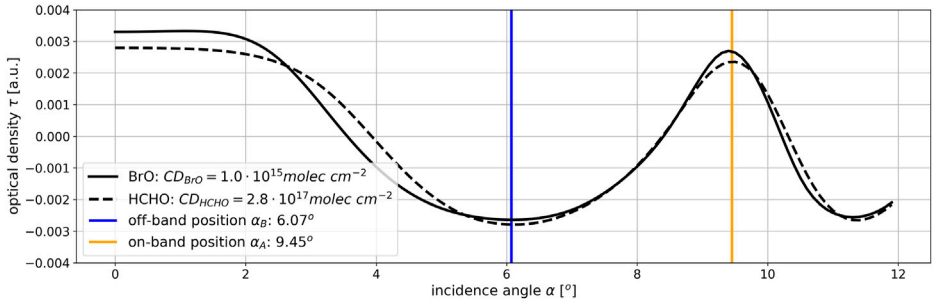

FIGURE 2
Modelled interferograms for BrO (CD_{BrO} = 1.0 × 10^{15} molec cm^{-2}) and HCHO (CD_{HCHO} = 2.8 × 10^{17} molec cm^{-2}). The BrO CD is chosen as atypical value for volcanic plumes and the HCHO CD is scaled according to have a similar absorption signal. The vertical lines show the on-band (orange line) and off-band (blue line) measurement angles for the BrO measurement. On-band and off-band measurement angles for BrO and HCHO are almost identical in the spectral region of the used bandpass filter.

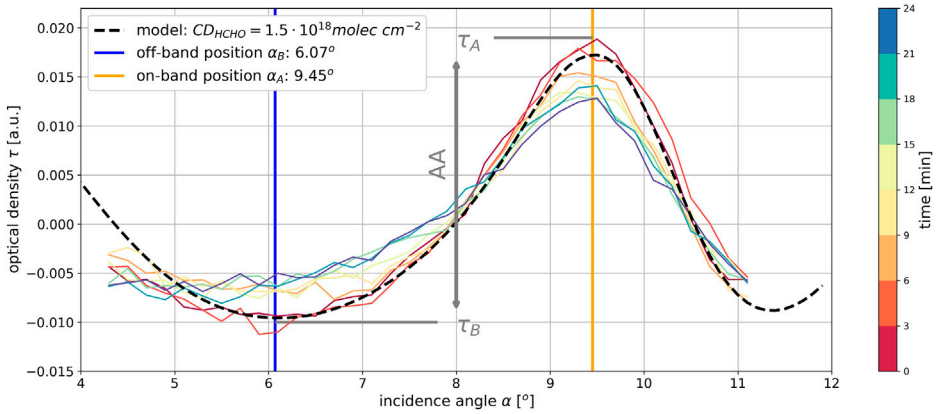

FIGURE 3
IFPICS interferogram of a HCHO gas cell, i.e., the optical density τ as a function of the FPI incidence (tilt) angle α, where the color scale indicates the time after initial heating of the HCHO gas cell. Since the gaseous HCHO repolymerizes to PFA during gas cell cooling, a decrease in AA signal (difference between τ_A and τ_B, see Section 2.3) is observed, which is indicated by the different colored lines. Black dashed line: model simulation for a HCHO CD of 1.5 × 10^{18} molec cm^{-2}. The measurement and the model simulation are normalized to their respective mean value. The vertical lines show the chosen on-band position α_A of 9.45° (orange) and off-band position α_B of 6.07° (blue) obtained from the comparison of measurement and model simulation.

FPI incidence angles and to avoid disturbing reflections for incidence angles lower than 4° inside the instrument optics on the detector (Fuchs et al., 2021). The results shown in Figure 3 yield the optimal angles α_A and α_B to achieve ideal on-band and off-band positions and show excellent agreement between the measurement and our model (dashed black line in Figure 3). The following FPI tilt angles optimizing the measurement of HCHO and BrO were used: an on-band position (A) of α_A = 9.45° and an off-band position (B) of α_B = 6.07°. The difference between minimum (τ_B) and maximum (τ_A) in this graph (vertical grey line) represents the AA, which is around 0.025. This is converted *via* a modelled calibration curve into a HCHO CD of 1.5 x 10^{18} molec cm^{-2}. The corresponding model interferogram is shown as the black dashed line in Figure 3. To illustrate the applicability of the IFPICS technique to imaging measurements of BrO, we show a measurement of two HCHO gas cells using scattered skylight as a light source in Figure 4A). The measurement is calibrated with a co-aligned narrow-FOV DOAS measurement, measuring the HCHO CD inside the smaller gas cell (see Figure 4B). The CD gained by the DOAS measurements is plotted as a function of IFPICS AA and fitted with a linear function, yielding a calibration curve for HCHO CDs. The measurement shows a nearly linear trend with increasing CD of the HCHO gas cells, but a deviation of approximately 17% to the model prediction for high HCHO optical densities is observed. Possible reasons are systematical errors in the DOAS evaluation due to the high HCHO optical densities, reflections at the cell (e.g., influencing the light path inside the cell), slight misalignments of the DOAS telescope optics and small errors introduced by the temperature dependence of the HCHO cross-section.

Instrument characterization measurements (such as the absolute calibration of the motor angle) are extremely simplified by

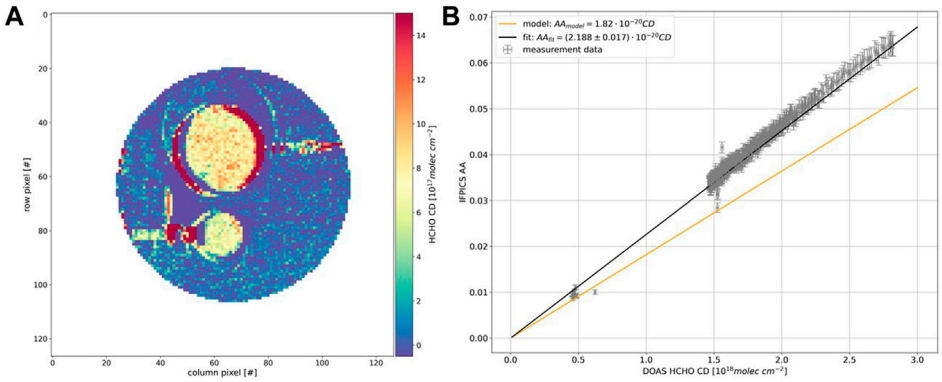

FIGURE 4
(A) Imaging measurement of two HCHO gas cells (Ø 50 mm and Ø 22 mm) with the IFPICS instrument from 19th of September 2020 at 08:03 UTC using scattered skylight as a light source. The measurement has a time resolution of 3 s and 8 × 8 pixel binning has been applied, resulting in an approximate spatial resolution of 80 × 80 pixels. The color scale shows the HCHO CD calibrated with a co-aligned DOAS measurement. **(B)** Calibration curve for the HCHO measurement shown in panel **(A)**. The DOAS instrument measures the CD inside the small gas cell and the DOAS calibration curve (black line) is compared to the model prediction (orange line). The gap between values around 5 × 10^{17} molec cm^{-2} and 1.5 × 10^{18} molec cm^{-2} originates from heating the gas cell, where the low CD measurements are prior to heating of the cell. The deviation between model prediction and measurement calibration is around 17%, possibly caused by errors in the DOAS evaluation, reflections at the cell, or slight misalignment of the DOAS telescope optics.

interferograms recorded with a gas cell with a high amount of the target trace gas (or a spectral tracer gas, like in our case HCHO). We note that the cross-sensitivity of our instrument to HCHO will generally have negligible impact on volcanic BrO measurements, since HCHO levels in volcanic plumes as well as background gradients within a typical instrument FOV are commonly low (typically below 10^{16} molec cm^{-2} corresponding to an optical density of 0.0002, see Figure 4B). Nevertheless, caution is necessary in regions with extensive biomass burning activities or wildfires. The applicability of the IFPICS technique to low differential optical densities (such as the BrO optical density of volcanic plumes, i.e., ca. 10^{-3}) has been shown by theoretical calculations of Kuhn et al., 2019. Furthermore, a more detailed investigation of the BrO camera prototype detection limit is shown in Supplementary Figures S1, S2. These laboratory studies show that gas cells with a high amount of HCHO can be used to characterize the BrO camera for volcanic applications.

3.2 Field campaign at Mt Etna July 2021

In order to test the performance of our instruments in the field we conducted simultaneous IFPICS measurements of BrO and SO_2 at Mt Etna volcano, Italy. The measurements were performed mainly during quiescent degassing periods.

3.2.1 15 July 2021: SO_2 flux measurements

The SO_2 flux measurement presented here was recorded on the 15th of July 2021 at the mountain ridge "Schiena dell'Asino" at a location of 37°42′35″ N 15°01′39″ E [1,900 m above sea level (a.s.l)] between 08:05 and 10:20 UTC. The camera points into a viewing direction of 327° N with an elevation angle of 20° in an approximate distance of 5.3 km to the crater area (see Figure 6B). The wind direction was 102° E with an approximate windspeed of 5 m s^{-1} (see Supplementary Figure S3). Images are taken with 1 s of exposure time, leading to a total image acquisition time for two consecutive images (with FPI setting A and B) of 2.3 s, because additional 0.3 s are lost due to movement of the stepper motor (tilting the FPI between on- and off-band position) and data acquisition.

The here presented SO_2 flux measurements illustrate the development of the SO_2 camera and flux calculations since Fuchs et al., 2021. With similar spatial resolution, higher frame rates (by about a factor of 2) are achieved through developments in the software and a more compatible detector (see Section 2.3). Figure 5A shows an exemplary image of the SO_2 CD inside the volcanic plume during the measurement period. A video of the complete measurement timeseries is included in the Supplementary Material. The SO_2 AA is calibrated using the instrument model (Section 2.3) and assuming an O_3 VCD of (312 ± 10) DU, obtained from TROPOMI satellite measurements (closest available data from the 24th of July 2021, see Geoservice 2022). The model accounts for the variation of the total O_3 column amount in the background spectrum introduced by the changing solar zenith angle (SZA, see also Fuchs et al., 2021). Figure 5B shows the model calibration curve for the beginning and the end of the measurement time series examined here. The calibration is performed dynamically according to actual SZA. The influence of O_3 on the sensitivity is similarly observed for traditional filter-based SO_2 cameras (Kern et al., 2010). But there it can only be corrected by frequent in-field calibration. The AA corresponding to the detection limit has a value 1.4 × 10^{-2} for an SZA of 55°, an integration time of 2.4 s and a spatial resolution of 400 × 400 pixel. We assume that the detection limit is determined by photon shot-noise, i.e., inversely proportional to the square exposure time. This corresponds to photon shot-noise limited detection limit of 4.7 × 10^{17} molec $s^{0.5}$ cm^{-2} normalized to 1 s of exposure time.

In order to calculate the SO_2 flux, the SO_2 CD is integrated along a transect of the plume (Supplementary Figure S4 and black

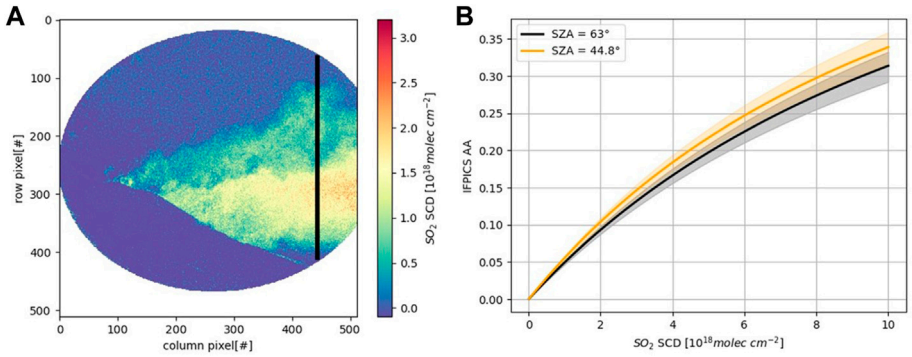

FIGURE 5
(A) SO_2 IFPICS image acquired at the 15th of July at the mountain ridge "Schiena dell'Asino" in an approximate distance of 5.3 km to the crater area. The image has a spatial resolution of 400 × 400 pixels and a time resolution of 2.4 s. The vertical black line shows the line of integration for the SO_2 flux calculation. **(B)** Exemplary model calibration curves of the SO_2 IFPICS instrument. The shaded area marks the model error. The black curve marks the first calibration (SZA = 63°) for the measurement time series and the orange curve the last one (SZA = 44.8°). In between the calibration curve is dynamically adapted according to the SZA.

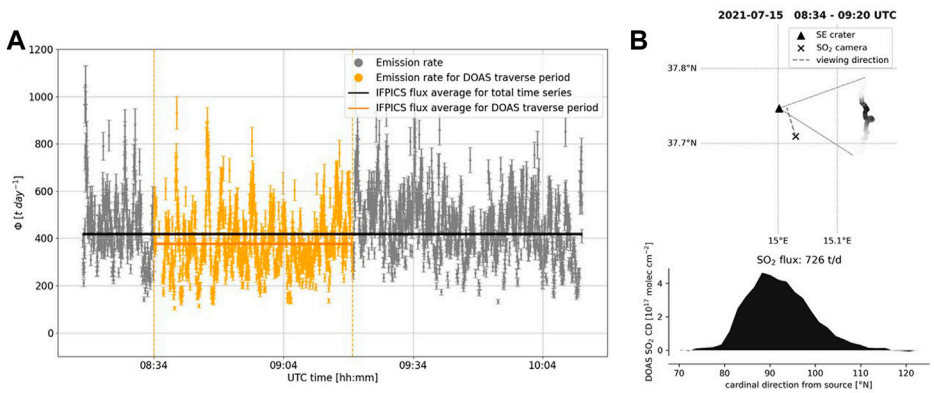

FIGURE 6
SO_2 flux measurements from 15th July 2021 (see Figure 5) **(A)** IFPICS SO_2 flux measured in an approximate distance of 5.3 km to the crater area of Mt Etna between 08:05 and 10:20 UTC. The orange part of the IFPICS data marks the time period of a DOAS car traverse measurement shown in panel **(B)**. The horizontal lines mark the average flux for the complete time series (black, (418 ± 138) t day^{-1}) and for the traverse time [orange, (378 ± 129) t day^{-1})]. **(B)** DOAS car traverse measurement of SO_2 flux between 08:34 and 09:20 UTC. The upper panel shows the location and direction of the plume and the viewing direction of the SO_2 camera. The lower panel shows the SO_2 CD during the plume traverse.

vertical line in Figure 5A and multiplied with the plume propagation velocity along the image plane (see Supplementary Figure S3). The plume's instantaneous propagation velocity (or the effective wind speed) is obtained by evaluating the optical flow field (using the algorithm by Farneback 2000) between two consecutive images at the transect of interest (see, e.g., Gliß et al., 2018). Figure 6A shows the resulting flux time series of the total emission of Mt Etna obtained on the 15th of July 2021 between 08:17 and 10:13 UTC. The mean flux for this timeframe is 418 t day^{-1} with a standard deviation of 138 t day^{-1}. The high frequency natural variability of the SO_2 emission is clearly visible and by far dominates the noise of the individual measurements (which amounts to a relative error of about 10%). The mean flux is compared to a DOAS car traverse measurement which was recorded during the IFPICS measurement timeseries between 08:34 and 09:20 UTC (see Figure 6B). This time period is marked by orange color in Figure 6A. The volcanic SO_2 emission flux determined by the DOAS car traverse is 726 t day^{-1}. It was calculated using the average plume propagation velocity obtained by the IFPICS measurement during the traverse period. The deviation by almost a factor of two is likely to be introduced by the following effects: 1) The SO_2 camera measurement during that time only captured a part of the plume (a rather small but unknown part was masked by topography). 2) Radiative transfer effects, in particular light dilution (e.g., Kern et al., 2009; Campion et al., 2015) are not accounted for in our evaluations. As the SO_2 camera is further away from the plume (5.3 km) and operates at lower wavelength than the DOAS, this could partially account for the observed deviation. 3) The DOAS car traverse was recorded during a

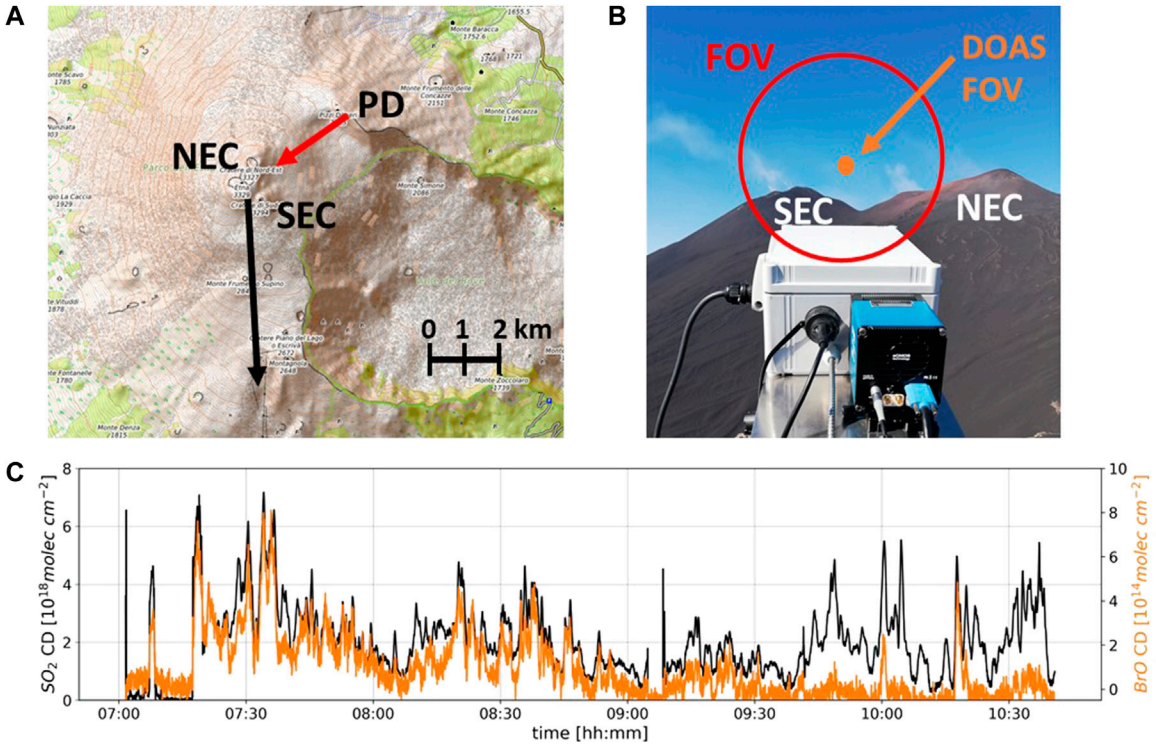

FIGURE 7
(A) Topographic map (OpenTopoMap, 2022) of the measurement location from 24th of July 2021, close to the Pizzi Deneri (PD) observatory, showing the viewing direction of the camera (205° SW, red arrow) and the plume direction (178° S, black arrow). Additionally, the South Eastern crater (SEC) and the North Eastern crater (NEC) of Mt Etna are marked. The measurement location has an approximate distance of 2.5 km to the crater area. **(B)** Image of the BrO camera with SEC and NEC in the background. The red circle marks the FOV of the camera. The plume is faintly visible between the two craters. The DOAS FOV is marked with an orange circle and it points directly into the plume. **(C)** Time series of the DOAS measurement (location marked with orange circle in panel B). The black line (left *y*-axis) shows the SO_2 CD and the orange line (right *y*-axis) the BrO CD between 07:00—10:30 UTC. BrO and SO_2 CDs are correlated up to approximately 10:45 UTC, when the plume shows a stronger condensation and also clouds start to form inside the plume.

rather long time (almost 30 min within the plume). During that time the plume might have slightly moved (e.g., meandering) in driving direction, which might have increased the apparent plume size.

3.2.2 24 July 2021: BrO and SO_2 measurements

For the BrO measurement we present a measurement from the 24th of July 2021 between 07:38 and 08:24 UTC which was recorded close to the Osservatorio Vulcanologico Pizzi Deneri at a location of 37°45′48″ N and 15°01′12″ E (ca. 2,800 m a.s.l., see Figure 7). The SO_2 and the BrO cameras were pointed towards the crater area at an approximate distance of 2.5 km. The centers of the FOVs were aligned in a direction of 205° SW with an elevation angle of 18° for the BrO camera and 15° for the SO_2 camera. The wind direction was 178° S with a wind speed of approximately 6 m s^{-1} (IFPICS optical flow retrieval, see Section 3.2.1). Measurements were performed nearly simultaneously with an exposure time of 0.3 s per image for the BrO camera and 1 s per image for the SO_2-camera. The integration time difference originates from the different skylight radiance in the respective operating wavelength ranges. A narrow-FOV DOAS measurement was performed simultaneously in the FOV of the BrO camera (see Figure 7B).

3.2.2.1 BrO detection

In order to reduce photon shot noise up to an AA of 10^{-3}, which corresponds to a detection limit of ca. 1×10^{14} molec cm^{-2}, 10 consecutively recorded measurement images are co-added and a spatial binning of 8×8 pixels is applied resulting in a temporal resolution of 10 s and a spatial resolution of approximately 200 × 200 pixels with a size of 3.7×3.7 m^2 per pixel at the distance of the plume (2.5 km). A detailed investigation of the detection limit of the BrO camera is shown in Supplementary Figures S1, S2. The narrow-FOV DOAS time series (Figure 7C) shows BrO column densities that range up to 1×10^{15} molec cm^{-2}, this corresponds to an approximate signal to noise ratio (SNR) of 10. Figure 8A shows an exemplary image of the BrO CD inside the volcanic plume. In fact, the plume is clearly distinguishable from the atmospheric background and the crater flank from the southeast crater of Mt Etna (see Figure 8B). The image is calibrated using the narrow-FOV DOAS measurement within the FOV of the camera (see Luebcke et al., 2013; Sihler et al., 2017), which is shown in Figure 9. Fitting of the calibration curve is performed with an orthogonal distance regression method (Boggs & Rogers 1990) from the SciPy python library (Virtanen et al., 2020), which considers errors in x-and *y*-direction. The DOAS calibration curve (black line in Figure 9)

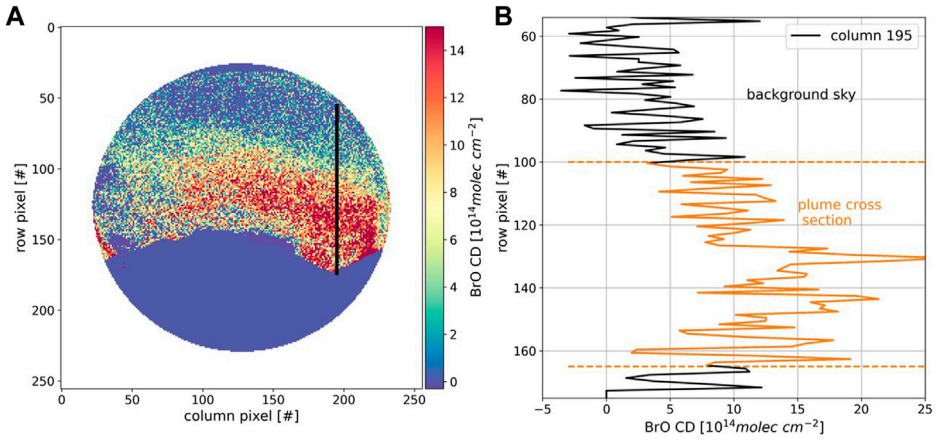

FIGURE 8
(A) BrO CD measured with the IFPICS prototype instrument and calibrated with the linear part of the narrow-FOV DOAS measurement (see Figure 7B and Figure 9). The image has a spatial resolution of 200 × 200 pixels and a time resolution of 10 s. The area of the crater flank is masked and set to zero to enhance the contrast between sky, plume and the crater flank. **(B)** Exemplary plot of column 195 [indicated as black line in **(A)**] from image. The volcanic plume signal (between row 100 and 165) in the range of 1.2 × 10^{15} molec cm^{-2} is clearly distinguishable from the background.

gives a slope of k_{IFPICS} = (5.50 ± 0.85) × 10^{-18} cm^2 $molec^{-1}$ which is in good agreement with the model prediction of k_{model} = 5.288 × 10^{-18} cm^2 $molec^{-1}$ (orange line in Figure 9). While the slope represents the expected BrO sensitivity of the instrument, we observe an apparently constant offset between the BrO CD determined by DOAS and that determined by the IFPICS technique (i.e., the BrO camera). Since the background sky is set to zero BrO by subtracting a mean value of the plume-free sky background in the IFPICS evaluation it is very likely that the effect causing the offset is due to some kind of interference within the volcanic plume (Supplementary Figure S2 shows that the background sky has a flat distribution on the order of 10^{-3}). This interference could be due to 1) unrecognized trace gases or 2) radiation transport effects. The influence of possible cross interferences of other gaseous absorbers was thoroughly studied by Kuhn et al., 2019 and are not plausible on the observed scale (extremely high HCHO levels can be ruled out on the basis of data from the narrow-FOV DOAS). However, since the plume was slightly condensed (visible but not opaque, Figure 7B) the offset could be due to radiative transfer changes introduced by the plume, i.e., scattering at plume aerosol leads to significant different atmospheric light paths for the plume and the background sky. The influence of light path enhancement (or shortening) on the measured CD is the same for IFPICS and DOAS. Differences in inelastic scattering effects (Grainger & Ring 1962) between plume and background sky are accounted for by the DOAS measurement (by the well-known procedure of adding a pseudo "Ring" absorber to the fit). However, they are presently ignored by the evaluation procedure of the IFPICS technique. This limitation restricts measurements with the present BrO camera prototype to aerosol-free plumes and demands further studies that quantify influences such as the differential Ring effect (Grainger & Ring 1962) between plume and background sky for the IFPICS technique. Nevertheless, the detection limit of the BrO camera (for aerosol-free conditions) can be estimated by the investigation of the 1-σ-pixel-pixel standard deviation in a plume free region of the background sky. This analysis was performed for a range of temporal (1 s–100 s) and spatial (no binning—32 × 32 pixel binning) binning parameters to optimize the trade-off between temporal and spatial resolution and the necessary reduction in photon shot-noise (see Supplementary Figure S1). For a spatial resolution of ca. 200 × 200 pixels (8 × 8 binning) and 10 s integration time the 1-σ-pixel-pixel standard deviation of the AA within the background sky is 1.5 × 10^{-3}. According to the calibration, this corresponds to a BrO CD of 2.8 × 10^{14} molec cm^{-2}. Consequently, the detection limit normalized to 1 s exposure is 8.9 × 10^{14} molec $s^{0.5}$ cm^{-2}, which closely matches the theoretical prediction of Kuhn et al., 2019.

3.2.2.2 BrO/SO_2 ratio

The BrO/SO_2 ratio is commonly observed in many volcanic plumes, for instance by the NOVAC network (e.g., Luebcke et al., 2014; Dinger et al., 2021). Since SO_2 can serve as a quasi-conservative tracer for dilution this ratio can give important insights in plume chemistry (von Glasow et al., 2009) but can be also related to volcanic activity (e.g., Warnach et al., 2019). Imaging measurements of this ratio can help to understand the complex chemical conversion mechanism within early plume stages, which is so far not well understood (see, e.g., Kuhn et al., 2022).

The BrO/SO_2 ratio inside the plume determined with the IFPICS measurements is compared to the narrow-FOV DOAS measurement inside the cameras FOV. Figure 10 shows a comparison of the BrO and SO_2 camera images. Both images are scaled to the same resolution and tailored to share approximately the same FOV. Despite the lower SNR of the BrO image (Figure 10A), the outline of the plume is well matched to the SO_2 image (Figure 10B). Furthermore, the instruments operate at different time resolutions. To account for this effect, the BrO and SO_2 time series from the DOAS measurement are individually compared to the respective IFPICS signals to obtain the FOV of the DOAS instrument within the IFPICS FOV(Sihler et al., 2017).

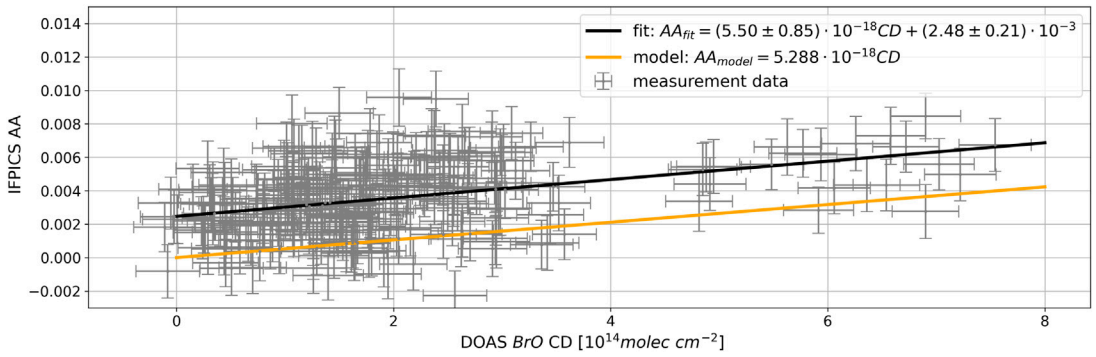

FIGURE 9
Calibration curve of the BrO measurement on the 24th of July 2021 between 07:38 and 08:24 UTC. The IFPICS AA inside the FOV of the narrow FOV DOAS is plotted against the BrO CD density obtained from the DOAS measurement. A linear fit (solid black line) gives the calibration curve of the BrO camera. The solid orange line shows the IFPICS model prediction.

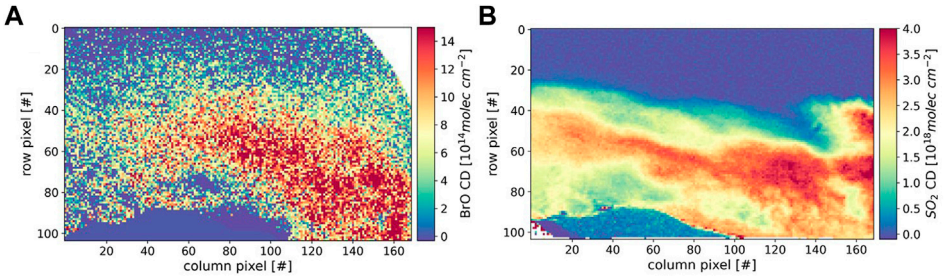

FIGURE 10
Cutout of BrO and SO_2 images acquired at the 24th of July with the IFPICS instruments. The plume originating from the Bocca Nuova crater moves from right to left through the image above the south eastern crater of Mt Etna. Panel **(A)** shows the BrO camera image and panel **(B)** the SO_2 camera image. The images are cutout to show the same FOV and scaled to have a similar temporal (10 s) and spatial resolution (104 × 169 pixels).

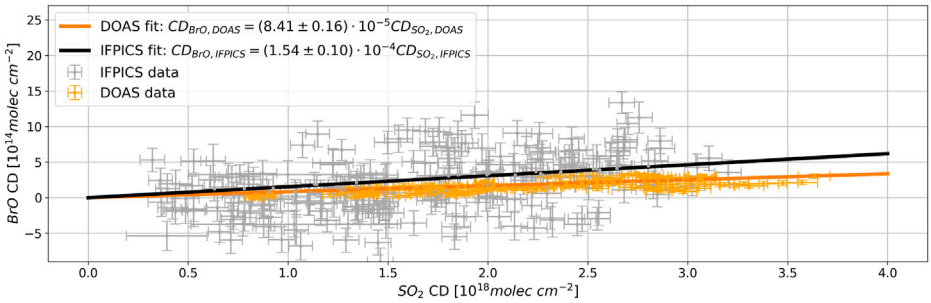

FIGURE 11
BrO/SO_2 ratio calculated from both instruments for the time period between 07:38 and 08:24 UTC. The pixels compared correspond to the FOV of the infield DOAS. The orange points show the infield DOAS measurement fitted with a linear function (solid orange line). The grey points mark the IFPICS measurement evaluated in the infield DOAS FOV also fitted with a linear function (black solid line).

The resulting BrO and SO_2 column densities at the IFPICS pixels corresponding to the DOAS FOV are calibrated with the IFPICS instrument model, interpolated to the time resolution of the BrO measurement and plotted in a scatter plot to retrieve the BrO/SO_2 ratio seen by the IFPICS instruments. In the calibration the offset in the BrO IFPICS data is subtracted (see Figure 9). The result is shown in Figure 11 (grey dots) and fitted with a linear function (solid black line) resulting in a BrO/SO_2 ratio of (8.41 ± 0.16) x 10^{-5} with a correlation coefficient of R = 0.37. This ratio is compared to the DOAS measurement of the BrO/SO_2 ratio (orange color in

Figure 11) which gives a value of $(1.54 \pm 0.10) \times 10^{-4}$ with a correlation coefficient of R = 0.90. The error of the slope is given as the standard deviation of the estimate. The values have a factor of 1.5 difference probably due to uncertainties in the alignment of the FOVs, the DOAS FOV retrieval and interpolation to account for different time resolutions. Nevertheless, the retrieved BrO/SO_2 ratio is comparable to previous measurements at Mt Etna (e.g., Bobrowski & Platt 2007). Future studies should also allow for two-dimensional BrO/SO_2 ratios, by improving the alignment of the FOVs of the IFPICS instruments under field conditions and optimization of the image evaluation.

4 Discussion and conclusion

Imaging of weakly absorbing trace gases in the atmosphere remains a challenging task. In this work, we showed that the IFPICS technique enables imaging remote sensing measurements of volcanic plume constituents other than SO_2. Imaging measurements of HCHO gas cells excellently matched the model predictions and first attempts to measure weak absorbers like BrO in the field showed promising results.

The determined detection limit of 2.8×10^{14} molec cm^{-2} for an exposure time of 10 s (corresponding to a differential optical density of approximately 1.5×10^{-3} for 10 s exposure time, two orders of magnitude smaller compared to common SO_2 measurements) is in good accordance with the performance expected from theoretical calculations (Kuhn et al., 2019). Moreover, field data of the IFPICS BrO AA confirm the modeled sensitivity when compared with DOAS measurements. However, for the presented measurement, we still observe a seemingly constant offset between the BrO data retrieved with DOAS and IFPICS, respectively. This offset is likely to indicate disturbing influences rooted in light path differences between (condensed) plume and blue sky background. In particular, the influence of, for instance, the differential Ring effect between plume and background sky needs to be investigated in future studies and might be reduced by adding additional wavelength channels. In the present state, the IFPICS BrO camera should only be applied to aerosol-free volcanic emissions.

We present advances in SO_2 flux measurements with the IFPICS technique. The flux difference found between DOAS car traverse measurement and the SO_2 camera in the presented example can be explained by not covering the whole plume in the camera FOV, radiative transfer effects and plume movements during the traverse measurement. The drastically enhanced SO_2 selectivity of the IFPICS technique in comparison to filter-based SO_2 cameras and the high temporal resolution compared to DOAS measurements demonstrate the possibility to study the variability of the SO_2 emission flux on short timescales with high accuracy and enables the use of the technique for weak emitters.

In addition, parallel SO_2 and BrO images recorded at Mt Etna are evaluated to give a value of $(8.41 \pm 0.16) \times 10^{-5}$ on the BrO/SO_2 ratio. The factor of 1.5 difference compared to the DOAS measurement might be due to inelastic scattering effects (Grainger & Ring 1962) between plume and background sky which are accounted for by the DOAS measurement but not yet in the IFPICS measurement (causing a BrO offset), uncertainties in calibration of both instruments and also imperfect alignment of the two IFPICS instruments. Improvements in the individual measurements of BrO and SO_2, better alignment and extended studies of inelastic scattering will also be reflected in the ratio of both gases.

In following up measurements of this type there is a great potential to study the distribution of both species within volcanic plumes and thus allowing detailed studies of the combined effects of mixing (of ambient air and thus O_3 and hydrogen radicals into the plume) and chemistry (e.g., the formation of BrO by the bromine explosion mechanism and the destruction of O_3). Future studies will also include two-dimensional BrO/SO_2 ratios.

Similarities between the absorption features of HCHO and BrO in the UV around 340 nm limit the measurement to low backgrounds of the respective interfering species, but also allows to use HCHO measurements as a proxy for BrO in volcanic plumes, because it is easier to handle under laboratory conditions. Imaging of BrO distributions can be useful to study processes in other environments, e.g., the polar boundary layer or above salt lakes. In turn, the IFPICS BrO could be used to quantify higher HCHO amounts (e.g., wildfires) in low BrO environments.

Furthermore, several other trace gases which show nearly periodic patterns in their absorption cross section will be detectable with the IFPICS technology, for example, nitrogen dioxide (NO_2), chlorine dioxide (OClO) or iodine oxide (IO).

Data availability statement

The raw data supporting the conclusion of this article will be made available by the authors, without undue reservation.

Author contributions

JK, NB, and UP developed the research question. AN, JH, CF, JK, and NB conducted the field campaign. CF designed and constructed the instrument. AN and JH characterized the instruments. AN evaluated the data, and wrote the manuscript, with all authors contributing by revising it within several iterations.

Funding

Support from the Deutsche Forschungsgemeinschaft (project DFG PL 193/23-1) and Terrestrial and Magmatic Systems (TeMaS - collaborative effort of the Universities of Mainz, Heidelberg and Frankfurt) is gratefully acknowledged.

Acknowledgments

We would like to thank SLS Optics Ltd. for sharing their expertise in designing and manufacturing the etalons.

Conflict of interest

The authors declare that the research was conducted in the absence of any commercial or financial relationships that could be construed as a potential conflict of interest.

Publisher's note

Supplementary material

The Supplementary Material for this article can be found online at: https://www.frontiersin.org/articles/10.3389/feart.2023.1063922/full#supplementary-material

SUPPLEMENTARY FIGURE S1
Plot of the detection limit investigation of the BrO camera showing the 1-σ-pixel-pixel standard deviation of the IFPICS AA σ_{AA} in a plume-free background sky region as a function of the integration time. The right x-axis shows the BrO CD calibrated with the IFPICS model giving the detection limit of the BrO camera.

SUPPLEMENTARY FIGURE S2
Background measurement of the IFPICS BrO camera showing homogeneity of the background sky. **(A)** Image of the measurement conditions from 11 July 2021 at the southern side of Mt Etna at the "Piano Vetore" plateau (position of 37°41′37″ N and 14°58′45″ E). The distance to the crater area is approximately 6.3 km. The red circle marks the FOV of the IFPICS instrument and the black box marks the cutout shown in panel **(B)**. **(B)** IFPICS AA signal of the sky background for an image with a spatial resolution of 200 × 200 pixels and a time resolution of 10 s. **(C)** Exemplary plot of row 20, showing that the variation in the IFPICS AA is on the order of 10^{-3}.

SUPPLEMENTARY FIGURE S3
Plume propagation velocity vplume retrieved from the optical flow calculation between two consecutive SO_2 camera images for the time series shown in Figure 6A. The windspeed is determined pixelwise at the position of the plume transect (see vertical black line in Figure 5A).

SUPPLEMENTARY FIGURE S4
Integrated transect of the SO_2 CD (SO_2 CD multiplied with the plume cross section σ_{plume}) for the time period of the SO_2 flux measurement in Figure 6A. The orange points denote the measurements during the DOAS car traverse.

References

Barrie, L., Bottenheim, J. W., Schnell, R. C., Crutzen, P. J., and Rasmussen, R. A. (1988). Ozone destruction and photochemical reactions at polar sunrise in the lower Arctic atmosphere. *Nature* 334, 138–141. doi:10.1038/334138a0

Bluth, G., Shannon, J., Watson, I. P. I., and Realmuto, V. (2007). Development of an ultra-violet digital camera for volcanic SO_2 imaging. *J. Volcanol. Geotherm. Res.* 161, 47–56. doi:10.1016/j.jvolgeores.2006.11.004

Bobrowski, N., Hoenninger, G., Galle, B., and Platt, U. (2003). Detection of bromine monoxide in a volcanic plume. *Nature* 423, 273–276. doi:10.1038/nature01625

Bobrowski, N., and Platt, U. (2007). SO_2/BrO ratios studied in five volcanic plumes. *J. Volcanol. Geotherm. Res.* 166, 147–160. doi:10.1016/j.jvolgeores.2007.07.003

Bobrowski, N., von Glasow, R., Aiuppa, A., Inguaggiato, S., Louban, I., Ibrahim, O. W., et al. (2007). Reactive halogen chemistry in volcanic plumes. *JGR Atmos.* 112, D06311. doi:10.1029/2006jd007206

Boggs, J., and Rogers, J. (1990). "Orthogonal distance regression," in *Contemporary mathematics*, 186. s.l.:s.n., p.

Bogumil, K., Orphal, J., Homann, T., Voigt, S., Spietz, P., Fleischmann, O., et al. (2003). Measurements of molecular absorption spectra with the SCIAMACHY pre-flight model: Instrument characterization and reference data for atmospheric remote-sensing in the 230–2380 nm region. *J. Photochem. Photobiol. A Chem.* 157, 167–184. doi:10.1016/s1010-6030(03)00062-5

Campion, R., Delgado-Granados, H., and Mori, T. (2015). Image-based correction of the light dilution effect for SO_2 camera measurements. *J. Volcanol. Geotherm. Res.* 300, 48–57. doi:10.1016/j.jvolgeores.2015.01.004

Chance, K., and Kurucz, R. (2010). An improved high-resolution solar reference spectrum for earth's atmosphere measurements in the ultraviolet, visible, and near infrared. *J. Quantitative Spectrosc. Radiat. Transf.* 111, 1289–1295. doi:10.1016/j.jqsrt.2010.01.036

Chance, K., and Orphal, J. (2011). Revised ultraviolet absorption cross sections of H_2CO for the HITRAN database. *J. Quantitative Spectrosc. Radiat. Transf.* 112, 1509–1510. doi:10.1016/j.jqsrt.2011.02.002

Dinger, F., Kleinbek, T., Dörner, S., Bobrowski, N., Platt, U., Wagner, T., et al. (2021). SO_2 and BrO emissions of Masaya volcano from 2014 to 2020. *Atmos. Chem. Phys.* 21, 9367–9404. doi:10.5194/acp-21-9367-2021

Farneback, G. (2000). *Fast and accurate motion estimation using orientation tensors and parametric motion models*. s.l., s.n. 135–139.

Fleischmann, O., Hartmann, M., Burrows, J., and Orphal, J. (2004). New ultraviolet absorption cross-sections of BrO at atmospheric temperatures measured by time-windowing Fourier transform spectroscopy. *J. Photochem. Photobiol.* 168, 117–132. doi:10.1016/j.jphotochem.2004.03.026

Fuchs, C., Kuhn, J., Bobrowski, N., and Platt, U. (2021). Quantitative imaging of volcanic SO_2 plumes using Fabry–Pérot interferometer correlation spectroscopy. *Atmos. Meas. Tech.* 14, 295–307. doi:10.5194/amt-14-295-2021

Geoservice, E. (2022). Sentinel-5P TROPOMI L3 daily composites - EOC geoservices. [Online] Available at: https://geoservice.dlr.de/web/maps/s5p:tropomi:l3 (Accessed 10 08 2022).

Gliß, J., Strebel, K., Kylling, A., and Sudbo, A. (2018). Improved optical flow velocity analysis in SO_2 camera images of volcanic plumes – implications for emission-rate retrievals investigated at Mt Etna, Italy and Guallatiri, Chile. *Atmos. Meas. Tech.* 11 (2), 781–801. doi:10.5194/amt-11-781-2018

Grainger, J. F., and Ring, J. (1962). Anomalous fraunhofer line profiles. *Nature* 193, 762. doi:10.1038/193762a0

Kern, C., Deutschmann, T., Vogel, L., Wöhrbach, M., Wagner, T., and Platt, U. (2009). Radiative transfer corrections for accurate spectroscopic measurements of volcanic gas emissions. *Bull. Volcanol.* 72, 233–247. doi:10.1007/s00445-009-0313-7

Kern, C., Kick, F., Lübcke, P., Vogel, L., Wöhrbach, M., and Platt, U. (2010). Theoretical description of functionality, applications, and limitations of SO_2 cameras for remote sensing of volcanic plumes. *Atmos. Meas. Tech.* 3 (3), 733–749. doi:10.5194/amt-3-733-2010

Kuhn, J., Bobrowski, N., Lübcke, P., Vogel, L., and Platt, U. (2014). A Fabry–Perot interferometer-based camera for two-dimensional mapping of SO_2 distributions. *Atmos. Meas. Tech.* 7, 3705–3715. doi:10.5194/amt-7-3705-2014

Kuhn, J., Bobrowski, N., and Platt, U. (2022). The interface between magma and Earth's atmosphere. *Geochem. Geophys. Geosystems* 23 12. doi:10.1029/2022gc010671

Kuhn, J., Platt, U., Bobrowski, N., and Wagner, T. (2019). Towards imaging of atmospheric trace gases using Fabry–Pérot interferometer correlation spectroscopy in the UV and visible spectral range. *Atmos. Meas. Tech.* 12, 735–747. doi:10.5194/amt-12-735-2019

Lohberger, F., Hoenninger, G., and Platt, U. (2004). Ground-based imaging differential optical absorption spectroscopy of atmospheric gases. *Appl. Opt.* 43, 4711–4717. doi:10.1364/ao.43.004711

Louban, I., Bobrowski, N., Rouwet, D., Inguaggiato, S., and Platt, U. (2009). Imaging DOAS for volcanological applications. *Bull. Vulcanology* 71, 753–765. doi:10.1007/s00445-008-0262-6

Luebcke, P., Bobrowski, N., Arellano, S., Galle, B., Garzón, G., Vogel, L., et al. (2014). BrO/SO_2 molar ratios from scanning DOAS measurements in the NOVAC network. *Solid earth.* 5 (1), 409–425.

Luebcke, P., Bobrowski, N., Illing, S., Kern, C., Alvarez Nieves, J. M., Vogel, L., et al. (2013). On the absolute calibration of SO_2 cameras. *Atmos. Meas. Tech.* 6, 677–696. doi:10.5194/amt-6-677-2013

Mori, T., and Burton, M. (2006). The SO_2 camera: A simple, fast and cheap method for ground-based imaging of SO_2 in volcanic plumes. *Geophys. Res. Lett.* 33, L24804. doi:10.1029/2006gl027916

OpenTopoMap (2022). OpenTopoMap. [Online]. Available at: https://opentopomap.org/#map=14/37.74992/15.01702 (Accessed 19 April 2022).

Platt, U., and Bobrowski, N. (2015). "Quantification of volcanic reactive halogen emissions," in *Volcanism and global environmental change*. Editors A. Schmidt, K. Fristad, and L. Elkins-Tanton (Cambridge University Press), 115–132. s.l.

Platt, U., and Lehrer, E. (1997). *Arctic tropospheric ozone chemistry, ARCTOC*. Heidelberg: s.n: Final Report of the EU-Project EV5V-CT93-0318.

Platt, U., and Stutz, J. (2008). *Differential optical absorption spectroscopy* 1 ed. Heidelberg: Springer Berlin. s.l.

Serdyuchenko, A., Gorshelev, V., Weber, M., Chehade, W., and Burrows, J. P. (2014). High spectral resolution ozone absorption cross-sections – Part 2: Temperature dependence. *Atmos. Meas. Tech.* 7, 625–636. doi:10.5194/amt-7-625-2014

Sihler, H., Lübcke, P., Lang, R., Beirle, S., de Graaf, M., Hörmann, C., et al. (2017). In-operation field-of-view retrieval (IFR) for satellite and ground-based DOAS-type instruments applying coincident high-resolution imager data. *Atmos. Meas. Tech.* 10, 881–903. doi:10.5194/amt-10-881-2017

Stutz, J., Ackermann, D., Fast, J. D., and Barrie, L. (2002). Atmospheric reactive chlorine and bromine at the great salt lake, Utah. *Geophys. Res. Lett.* 29 (10), 18-1–18-4. doi:10.1029/2002gl014812

Vance, A., McGonigle, A. J. S., Aiuppa, A., Stith, J. L., Turnbull, K., and von Glasow, R. (2010). Ozone depletion in tropospheric volcanic plumes. *Geophys. Res. Lett.* 37 22. doi:10.1029/2010gl044997

Virtanen, P., Gommers, R., Oliphant, T. E., Haberland, M., Reddy, T., Cournapeau, D., et al. (2020). SciPy 1.0: Fundamental algorithms for scientific computing in Python. *Nat. Methods* 17 (3), 261–272. doi:10.1038/s41592-019-0686-2

von Glasow, R., Bobrowski, N., and Kern, C. (2009). The effects of volcanic eruptions on atmospheric chemistry. *Chem. Geol.* 263 (1 - 4), 131–142. doi:10.1016/j.chemgeo.2008.08.020

Warnach, S., Bobrowski, N., Hidalgo, S., Arellano, S., Sihler, H., Dinger, F., et al. (2019). Variation of the BrO/SO_2 molar ratio in the plume of tungurahua volcano between 2007 and 2017 and its relationship to volcanic activity. *Front. Earth Sci. Vulcanology* 7. doi:10.3389/feart.2019.00132